ORIGINAL PAPER

Finite element modeling of hydraulic fracturing in 3D

Magnus Wangen

Abstract A procedure based on the finite element method is suggested for modeling of 3D hydraulic fracturing in the subsurface. The proposed formulation partitions the stress field into the initial stress state and an additional stress state caused by pressure buildup. The additional stress is obtained as a solution of the Biot equations for coupled fluid flow and deformations in the rock. The fluid flow in the fracture is represented on a regular finite element grid by means of "fracture" porosity, which is the volume fraction of the fracture. The use of the fracture porosity allows for a uniform finite element formulation for the fracture and the rock, both with respect to fluid pressure and displacement. It is demonstrated how the fracture aperture is obtained from the displacement field. The model has a fracture criterion by means of a strain limit in each element. It is shown how this criterion scales with the element size. Fracturing becomes an intermittent process, and each event is followed by a pressure drop. A procedure is suggested for the computation of the pressure drop. Two examples of hydraulic fracturing are given, when the pressure buildup is from fluid injection by a well. One case is of a homogeneous rock, and the other case is an inhomogeneous rock. The fracture geometry, well pressure, new fracture area, and elastic energy released in each event are computed. The fracture geometry is three orthogonal fracture planes in the homogeneous case, and it is a branched fracture in the inhomogeneous case.

M. Wangen (✉)
Institute for Energy Technology,
P.O. Box 40, 2027 Kjeller, Norway
e-mail: Magnus.Wangen@ife.no

1 Introduction

Hydraulic fracturing is the coupled dynamics of fracture and fluid flow, where the rock fractures because of an increasing pore fluid pressure [17]. It is a process that is commonly used by the petroleum industry to enhance the flow properties of the near-well region [13]. The injection fluid often contains proppants that props up the fractures after the injection has stopped. Hydraulic fracturing is necessary in the production of the gas from low-permeability shales [6]. Another example is the use of hydraulic fracturing to create conductivity between injection and production wells in geothermal systems [10, 27]. Hydraulic fracturing can also have unwanted effects, like for instance, leakage of natural gas into the groundwater from shale gas operations [20]. Another example is safe storage of large quantities of CO_2, which requires injection scenarios that do not fracture the sealing rocks above the reservoir [21, 26]. It should be mentioned that hydraulic fracturing occurs naturally in the subsurface as a mechanism that releases fluids during pressure buildup over geological time [31, 37]. Other examples are melt segregation and eruption in the crust [16], melt intrusion as sills and dykes [32], mud volcanos, and hydrothermal megaplumes [18].

The propagation of hydraulic fractures can be observed with passive seismic monitoring, and the seismic events can be correlated with the well pressure and the injection rate [24, 28–30, 39]. Injection tests have shown a nearly flat well pressure for a constant injection rate [29, 30]. On the other hand, the same well pressure

curves have the expected fall-off shape when injection stops. The nearly flat well pressure observed during injection cannot easily be explained as compressible Darcy flow, in the same way as the fall-off curves. Seismic mapping shows that hydraulic fracturing is an intermittent process and that the events fill the length interval between the injection point and the seismicity front [25, 29]. Therefore, it is difficult to map the shape of the fracture. Another challenging aspect with respect to fracture modeling is the rough surfaces of the fracture walls and the non-evenly distributed flow between them [2, 3, 5].

There are several 3D models of hydraulic fracturing [7, 8, 22]. These modeling approaches have things in common in that they assume that fracturing takes place in a given plane, like for instance, the reservoir interval of a vertical plane through the injection point. The models are often based on analytical expressions for the coupling of fracture fluid pressure and the fracture width and the leak-off rate into the rock. They can be viewed as 3D extensions of the pioneering analytical 2D models of hydraulic fracturing, like the PKN- and the GDK-models; see Geertsma [12] for a review. There are also 3D models of hydraulic fracturing based on the distinct element method, where the forces on each grain in the rock ensemble is accounted for [1].

A finite element approach is here suggested for the modeling of hydraulic fracturing in 3D. The model is an extension to 3D of a similar model that was developed for 2D [38]. The model is based on the Biot equations for the deformations of the rock caused by gradients in the fluid pressure. The fracture is represented on the same regular grid as the rock by means of "fracture porosity," without any special regridding. The fracture porosity is the volume fraction of the fracture in a rock volume. It is possible, by means of the fracture porosity, to make a uniform finite element formulation for the rock and the fracture, both with respect to the fluid pressure and displacement. This model has a fracture criterion based on element strain. An element breaks, and the fracture propagates, when the strain computed at the center of an element exceeds a strain limit.

There are several new features in the 3D implementation, compared to its 2D predecessor. The failure criterion in 3D is based on the strain in the center of each element. The 2D model had a failure criterion based on the strain of the element sides, which are bonds that connect the nodes. This latter concept, which is widely used by simple fracture models in physics, does not easily generalize to 3D. It is now explained how the stress state is divided into an initial state that includes the gravity, and the difference from the initial state, which is caused by fluid injection from a well. It is

also explained how the full effective stress state can be used in a Mohr–Coulomb failure criterion. The fracture width is needed in the permeability function, and a procedure is suggested for obtaining the fracture width (aperture) from the displacement field for non-planar fractures. Finally, it is demonstrated that this approach works equally well in 3D as in 2D.

The paper is organized as follows: The partitioning of the stress into the initial stress state and the additional stress state caused by fluid injection is explained first. A presentation of Biot equations for the rock is followed by a derivation of the pressure equation for the fracture, and a discussion of the numerical solution of the coupled system of equations. The fracture criterion is presented, before a demonstration and validation are given for the computation of the fracture aperture. The pressure drop following a fracture event is explained, the scaling of the strain threshold with grid size is shown, before two case studies are presented— the hydraulic fracturing of a homogeneous rock and of an inhomogeneous rock.

2 The stress state

The stress in the rock is denoted by σ_{ij}, and it is a solution of the equilibrium equations

$$\frac{\partial \sigma_{ij}}{\partial x_j} = \varrho_b \, g \, \delta_{i3} \tag{1}$$

where ϱ_b is the bulk density of the rock and g is the gravitational acceleration [17]. The indices i and j run over the spatial directions, and they can be either x, y, and z, or 1, 2, and 3, where $x = 1$, $y = 2$, and $z = 3$. Einstein summation convention is applied by assuming summation over each pair of equal indices. The stress state in the subsurface is divided into two parts—the initial stress state $\sigma_{ij}^{(0)}$ and the difference from the initial state, $\sigma_{ij}^{(1)}$, which is caused by fluid injection. We, therefore, have that

$$\sigma_{ij} = \sigma_{ij}^{(0)} + \sigma_{ij}^{(1)}. \tag{2}$$

The initial stress state is a solution of the equilibrium Eq. 1, which also fulfills the boundary conditions before fluid injection starts.

We will not deal with what kind of rheology or processes that have caused the initial state of stress. It is taken to be the result of time- and temperature-dependent visco-plastic rheology that has been acting over millions of years. Furthermore, the rock is assumed to be initially free of elastic deformations. All elastic deformation is, therefore, the result of fluid

injection. We are, in this study, interested in tensile (mode I) hydraulic fracturing. The initial stress state is, therefore, taken to be isotropic, where the stress in the vertical direction is the weight of the overburden

$$\sigma_{zz}^{(0)} = \int_0^z \varrho_b(z) g \, dz \tag{3}$$

and where the initial stress in the horizontal plane is

$$\sigma_{xx}^{(0)} = \sigma_{yy}^{(0)} = A\sigma_{zz}^{(0)} \tag{4}$$

$$\sigma_{xy}^{(0)} = \sigma_{yz}^{(0)} = \sigma_{zx}^{(0)} = 0 \tag{5}$$

where $A = 1$. The surface is at $z = 0$. The initial stress state given by Eqs. 3 and 5 does not depend on the lateral position (x, y), and it is seen to be a trivial solution of the equilibrium equations. An anisotropic initial stress state, where $A \neq 1$, can lead to shear fracturing when the pore pressure increases. Then, the fracture condition is normally given by a Mohr–Coulomb fracture envelope.

Our concern here is the difference from the initial stress state caused by changes in the fluid pressure. It is straightforward to subtract the initial state of stress from the force balance Eq. 1, and we are then left if the following equilibrium equations for the stress difference

$$\frac{\partial \sigma_{ij}^{(1)}}{\partial x_j} = 0. \tag{6}$$

We notice that the effect of gravity resides entirely in the initial stress state. It is assumed that the boundaries are sufficiently far away from injection well to feel the effect of fluid injection. The stress at the boundaries therefore stays unchanged during the well operation. Boundary conditions for Eq. 6 are, therefore, a stress difference equal to zero.

3 The Biot equations for the rock

The initial stress state is the result of the geohistory, which includes a number of time- and temperature-dependent mechanical and chemical processes acting over millions of years. The changes in the stress state caused by well operations over a short time span, from minutes or hours to a few years, are assumed to follow Biot's poro-elastic equations for coupled fluid flow and deformations in porous media [4, 36]. The deformations are then caused by the effective stress defined as

$$\tau_{ij} = \sigma_{ij} - \alpha p_f \delta_{ij} \tag{7}$$

which is the stress σ_{ij} minus the pore fluid pressure p_f multiplied with the Biot coefficient α. The fluid pressure is now written as the sum of the initial fluid pressure $p^{(0)}$ and the difference from the initial fluid pressure, $p^{(1)}$, as

$$p_f = p^{(0)} + p^{(1)}. \tag{8}$$

The effective stress (7) can then be divided into two parts: one part with respect to the initial state and a second part that is the difference from the initial state:

$$\tau_{ij} = \left(\sigma_{ij}^{(0)} - \alpha p^{(0)}\delta_{ij}\right) + \left(\sigma_{ij}^{(1)} - \alpha p^{(1)}\delta_{ij}\right) \tag{9}$$

where $\tau_{ij}^{(0)} = \sigma_{ij}^{(0)} - \alpha p^{(0)}\delta_{ij}$ is the effective stress in the initial state and where $\tau_{ij}^{(1)} = \sigma_{ij}^{(1)} - \alpha p^{(1)}\delta_{ij}$ is the effective stress caused by recent changes in the fluid pressure. We are interested in the deformations caused by the difference in effective stress from the initial state. Poro-elasticity relates these deformations to the Lamé equations:

$$\tau_{ij}^{(1)} = -\left(\lambda \epsilon_{kk}\delta_{ij} + 2G\epsilon_{ij}\right) \tag{10}$$

where ϵ_{ij} is the strain

$$\epsilon_{ij} = \frac{1}{2}\left(\frac{\partial u_i}{\partial x_j} + \frac{\partial u_j}{\partial x_i}\right) \tag{11}$$

and where u_i is the displacement in the i-direction [17]. The minus sign is introduced in the stress–strain relation (10) in order to have compression corresponding to positive effective stress and tension to negative effective stress. The Lamé parameters λ and G are given by Young's modulus E and Poisson ratio ν as

$$\lambda = \frac{\nu E}{(1+\nu)(1-2\nu)} \quad \text{and} \quad G = \frac{E}{2(1+\nu)}. \tag{12}$$

Inserting the stress difference

$$\sigma_{ij}^{(1)} = -\left(\lambda \epsilon_{kk}\delta_{ij} + 2G\epsilon_{ij}\right) + \alpha p^{(1)}\delta_{ij} \tag{13}$$

into the equilibrium Eq. 6 together with the strain (11) gives the equation for the displacement field

$$\left(\lambda + G\right)\frac{\partial^2 u_k}{\partial x_k \partial x_i} + G\frac{\partial^2 u_i}{\partial x_k \partial x_k} = \alpha \frac{\partial p^{(1)}}{\partial x_i}. \tag{14}$$

This equation shows that the displacements in the rock are caused by the gradient of the pressure difference $p^{(1)}$. Another point is that Eq. 14 has no explicit time dependence. The time dependence follows from the implicit time dependence of the pressure.

The displacement field need to be specified for at least one node in order to make a numerical solution. Fixed nodes (zero displacement) at the four corner nodes of the surface plane are used in the current numerical implementation.

4 The pressure equation

The equation for the fluid pressure in the Biot model is [4, 36]

$$S\frac{\partial p}{\partial t} - \nabla\left(\frac{k}{\mu}(\nabla p - \varrho_f g\,\mathbf{n}_z)\right) = -\alpha\frac{\partial\epsilon}{\partial t} \qquad (15)$$

where S is the specific storage coefficient, $\epsilon = \epsilon_{11} + \epsilon_{22} + \epsilon_{33}$ is the volume strain, k is the permeability, and μ the viscosity. The initial fluid pressure is now taken to be hydrostatic:

$$p^{(0)} = \int_0^z \varrho_f g\,\mathrm{d}z \qquad (16)$$

where the basin has a horizontal surface at zero hydrostatic pressure. Inserting the pressure (8) into the Eq. 15 gives a pressure equation for $p^{(1)}$ as

$$S\frac{\partial p^{(1)}}{\partial t} - \nabla\left(\frac{k}{\mu}\nabla p^{(1)}\right) = -\alpha\frac{\partial\epsilon}{\partial t} \qquad (17)$$

The pressure equation is solved with zero initial pressure. Boundary conditions have zero pressure at the top surface and with all other boundaries closed for fluid flow.

We noticed from the Lamé Eq. 10 that non-zero displacements result from the pressure gradient $\nabla p^{(1)}$. The pressure Eq. 15 shows that changes in the volume strain act as a source term for fluid pressure.

The Appendix gives the details of the finite element formation of Lamé Eq. 10 and the pressure Eq. 17.

5 A pressure equation for the fracture

The pressure Eq. 15 covers only intact rock, not the fracture. An expression for conservation of fluid mass in the fracture is the starting point for a pressure equation that covers the broken elements. Figure 1 shows a regular grid with a fracture and the fractured elements. The mass balance for fluid in the fracture is

$$\frac{d}{dt}\int_{V_F}\varrho_f\,\mathrm{d}V + \int_{\partial V_F}\varrho_f\mathbf{v}_D\cdot\mathbf{n}\,\mathrm{d}A = \dot{M}_{\mathrm{in}} \qquad (18)$$

where V_F is the fracture volume, $\mathbf{n}$ is the outward unit normal vector on V_F and where $\dot{M}_{\mathrm{in}}$ is the mass rate of injection. The injection term $\dot{M}_{\mathrm{in}}$ is equal to the leak-off through the fracture walls (second term on left-hand side) added to the rate of change of fluid mass stored in the fracture (first term on the left-hand side). The mass balance (18) has two end-members, where one is an impermeable rock and the other is a permeable rock. There is no leak-off from the fracture in the impermeable case, and the second term in Eq. 18
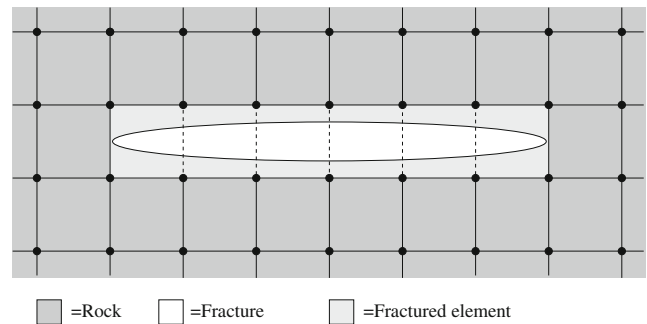

 =Rock   =Fracture   =Fractured element

Fig. 1 Representation of the fracture by a regular finite element grid

is zero. The injection rate is therefore equal to the rate of storage in the fracture. The opposite case is a permeable rock, where the leak-off dominates the storage rate. The leak-off in this case is almost the same as the injection rate.

The mass balance for fluid in the fracture can also be written for a single fractured element as

$$\frac{d}{dt}\int_{V_E}\phi_F\varrho_f\,\mathrm{d}V + \int_{\partial V_E}\varrho_f\mathbf{v}_D\cdot\mathbf{n}\,\mathrm{d}A = \dot{M}_E \qquad (19)$$

where V_E is the volume of the element, $\dot{M}_E$ is an eventual source/sink term, $\mathbf{n}$ is the outward unit normal vector of the element, and where ϕ_F is the sum of the element porosity and the "fracture porosity." The fracture porosity is the volume of the fracture within the element divided by the element volume (V_F/V_E), and ϕ_F becomes

$$\phi_F = \phi + \frac{V_F}{V_E}. \qquad (20)$$

The fracture volume is obtained as $V_F = V_E' - V_E$, where V_E' is the element volume when the displacement field is added (V_E is the volume of the unloaded element). The time-derivation goes through the integration sign in Eq. 19, because the element volume V_E is constant. The Gauss theorem converts the surface integral in Eq. 19 to a volume integral, which then gives the following pressure equation for the fractured elements:

$$\phi_F c_f\frac{\partial p}{\partial t} - \nabla\left(\frac{k_F}{\mu}\nabla p\right) = -\partial\phi_F/\partial t \qquad (21)$$

where c_f is the fluid compressibility. The well element has, in addition, a source term Q_{in}/V_E, where Q_{in} is the injection rate (fluid volume per time). The volume flux along the fracture is now given by the Darcy flux from fractured to non-fractured elements.

The permeability of the fractured elements is the arithmetic mean of the rock permeability and the

parallel plate permeability $k_p = w^2/12$, where w is the average aperture of the element. The extension of an element is found for all three spatial directions. The maximum opening is used in the permeability function, when an element is extended in more than one direction. The average permeability is taken to be scalar, which normally assures good communications along the fractures, even in the case of a corner element in a right-angled bend.

6 The coupling of pressure and displacement

The pressure and displacement equations are solved decoupled (or sequential) since that gives a simple numerical formulation and a large computational gain compared with a fully coupled numerical solution. On the other hand, a decoupled (or sequential) approach may lead to an instable formulation [19]. It is the source term $\alpha \, \partial \epsilon / \partial t$ in the pressure Eq. 17 that may lead to instability problems if the flow and the mechanics are tightly coupled. This may be the case for the fractured elements that are assigned a very low or a zero Young's modulus.

In the current applications, we are interested in hydraulic fracturing by fluid injection. The fluid pressure and the fluid flow in the fracture are then dominated by the injection rate from the well element. The fluid pressure will be nearly constant in the fracture in case of a "large" fracture permeability. The source term $\alpha \, \partial \epsilon / \partial t$, which accounts for storage of fluid in the fracture, represents a negligible volume rate when compared to the volume flow in the fracture that leaks off into the rock.

A simple way to achieve unconditional stability is to approximate the source term by zero ($\alpha \, \partial \epsilon / \partial t \approx 0$) for all elements. The displacement field then becomes a slave of the pressure field. One could restrict the approximation to only the fractured elements, but numerical testing indicates that this term has negligible impact on the results compared to the parameters that control the intermittent nature of the growth of the fracture. The main feedback from the displacement on the pressure is the fracture propagation.

This approximation is inappropriate for an impermeable rock or extremely low permeable rock, where very little or no fluid leaks off into the rock and where most of the injected volume remains in the fracture.

There are several ways to implement numerically the sequential coupling of pressure and displacement equations. Kim et al. [19] analyze the stability of four different schemes for sequential coupling. They strongly recommend the "fixed stress" sequential method, where the flow problem is solved first with a frozen total mean stress field.

7 Fracture criterion

Fracture nucleation, propagation, and interaction in heterogeneous media have been studied with simple models like the random fuse model and models made of springs and beams; see Herrmann and Roux [14] for a review. These models have later evolved into the beam model and the spring model of hydraulic fracturing, [33–35] and [11], respectively. The material strength in these models is represented by the strength of bonds like fuses, springs, and beams. It is, therefore, easy to represent heterogeneous materials with these models.

A 2D finite element model of hydraulic fracturing, based on the Biot equations for the rock, which is using bond strength, was proposed by Wangen [38]. The sides of the finite elements define the bonds, and they have a strength threshold in terms of strain, just as for springs and beams. A bond will break when it is stretched beyond its strength threshold. The use of the element sides as bonds makes fracture propagation straightforward in 2D, because a broken bond opens the fracture into a new element.

Element sides used as bonds in 2D do not easily generalize to 3D, since an element side is an area in 3D. An alternative to "bond" strength is a strain threshold assigned directly to the elements. The fracture criterion is formulated as

$$\max(\epsilon_{xx}, \epsilon_{yy}, \epsilon_{zz}) \geq \epsilon_{\text{frac}}, \tag{22}$$

where ϵ_{frac} is the strain threshold and where the strain is computed at the center of the element. The strength threshold will be the same in all directions in case of isotropic rock properties. An element gets almost zero Young's modulus, fracture permeability, and fracture porosity when it changes state from rock to fracture.

The propagation of one fracture can be modeled by looping over all nearest neighbor elements to the fracture. The overstretched neighbor elements break and become a part of the fracture. Testing shows that this criterion gives similar results as the bond-strength criterion when applied to 2D.

The criterion (22) does not represent shear fractures, although shear strain could be the result of stress interactions of a branched fracture. It is possible to introduce a Mohr–Coulomb failure criterion and allow for shear fractures. Such a criterion is straightforward to implement on an element basis, where the effective stress at the center of the element decides if shear fracture takes place.

It is worth noting that a Mohr–Coulomb failure criterion is based on the full effective stress, $\tau_{ij} = \tau_{ij}^{(0)} + \tau_{ij}^{(1)}$, which involves the initial stress and pressure states. The Mohr–Coulomb failure criterion then generates tensile fracture in a plane that is normal to the least compressive stress. The modeling becomes simplified if the Cartesian coordinate system is aligned with the principal stress directions. Shear fracture will not be discussed any further in this study, since it is restricted to tensile fracturing.

8 Validation of the stress solution

A fluid pressure in a flat fracture pushes the fracture walls apart. There is a simple analytical solution for the aperture in case of a circular fracture in an infinite, impermeable, and linear elastic rock. The fracture then becomes an ellipsoid with the aperture given as follows:

$$w(r) = w_{max} \sqrt{1 - (r/a)^2} \qquad \text{and}$$

$$w_{max} = \frac{2(1 - \nu)pa}{\pi G} \tag{23}$$

where w_{max} is the maximum aperture at its center when p is a constant fluid pressure in the fracture [17]. The fracture has the radius a, and the radial position from its center is r. This is the case of an impermeable rock, with zero leak-off, where the fluid pressure is zero everywhere in the pore space, but non-zero at the fracture walls. Figure 2 shows the results of a numerical computation of the fracture surface when $a = 15$ m, $E = 50$ GPa, $\nu = 0.25$, and fracture pressure $p = 100$ MPa. The plotted surface is the z-coordinate added to the displacement field $u_z = w(r)$. The aperture is obtained from the displacement field of the nodes of the fracture surface on the regular grid. The figure shows the fracture surface when the displacement field
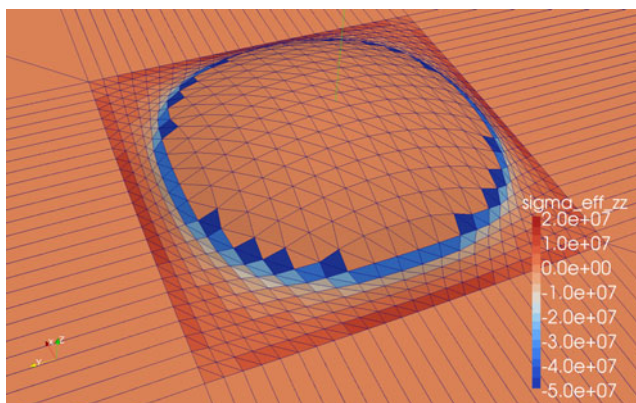
is multiplied by a suitable factor to clearly show the ellipsoid. A comparison of the numerical solution and the exact ellipsoid solution (23) is shown in Fig. 3. The figure compares the numerical displacement field and the exact one for a vertical plane through the center of the fracture. The comparison is good although it is not exact. Higher resolution and better griding could have improved the match.

The fracture walls are obtained by moving the displacement field to the center of element. Figure 3 shows that the numerically computed displacement field gives the aperture and the fracture shape, even though the fracture is represented by elements of a regular grid with macroscopic or mesoscopic size. The aperture was computed using an element thickness of 2 m. Figure 2 also shows the stress enhancement for the elements at the tip of the fracture.

The numerical pressure solution has been tested separately, by comparing it with Theis time-dependent solution for well pressure [38]. It is difficult to validate the dynamical behavior of the model because of intermittent fracturing. Analytical models or semi-analytical models for hydraulic fracturing have a continuous fracture growth. Continuous fracture growth gives that fracture properties like length, width, and pressure are proportional to $(\text{time})^n$ where n is a model- and property-dependent exponent. These exponents are in the range between 0 and 1, and the exponents for length and width add up to 1 for models with zero or little
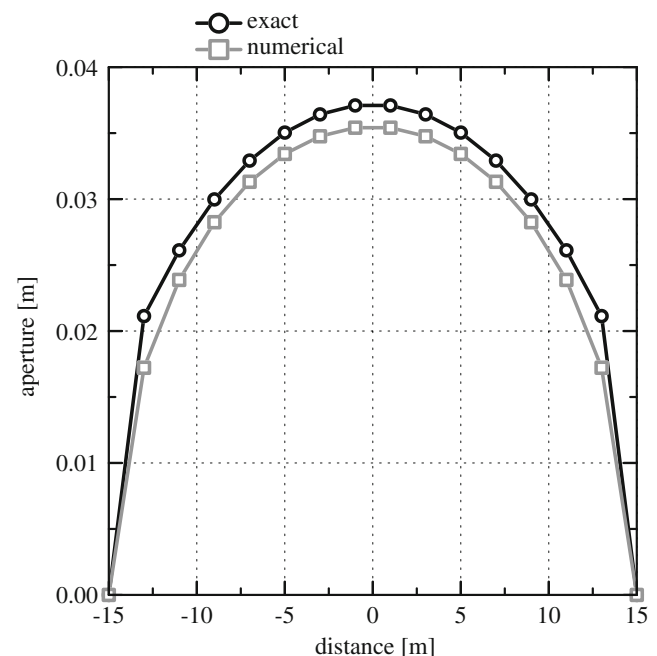

Fig. 2 Fracture surface from constant fracture pressure

Fig. 3 Displacement field through the ellipsoid in Fig. 2

leak-off [9]. It is uncertain how one could make the current model approach, the continuous models, with their assumptions in order to compare the dynamical behavior.

9 Pressure drop during fracture propagation

Fracturing and the fracture propagation are assumed to take place instantaneously. The volume of fluid in the fracture is, therefore, the same right after a fracture event as it was right before. Fracture propagation leads to a larger fracture surface, and a lower fluid pressure is therefore needed to keep the fracture open. A constant fluid volume in the fracture implies that an increasing fracture surface gives a reduced fracture aperture. It is, therefore, an instant pressure drop in the fracture following propagation.

It is possible to compute the fracture volume and, thereby, the pressure drop that follows a fracture event. We assume that the fracture is sufficiently permeable, for variations in the fluid pressure inside the fracture to be small. A constant fluid pressure is assigned to the nodes along the fracture surface. The equilibrium equations are solved for the displacement field. The displacement field at the nodes is used to compute the volume change of the elements. The total fracture volume is the volume difference between the current and the initial state of the fractured elements. The fracture volume must remain unchanged for an event if the fluid volume is unchanged, assuming that the fluid fills the fracture completely. A Newton scheme is used to compute the pressure drop in the fracture. Just two iterations are normally needed because the fracture volume and the fracture fluid pressure are almost linearly related.

10 Strain threshold and grid size

The fracture criterion (22) is by means of strain computed in the center of the elements. If the strain in an element exceeds the breaking threshold, as given by Eq. 22, the element then changes properties from rock to fracture. The most strained elements are the ones at the tip of a fracture, as shown in Fig. 2. Figure 4 shows the strain (ϵ_{yy}) and the effective stress (τ_{yy}) at the tip of a 2D linear fracture aligned with the x-direction. There is a clear enhancement of the strain and the effective stress in the element at the fracture tip.

The strain and the effective stress at the fracture tip is dependent on the element size. How stress and strain scale with the element size is studied numerically using square elements of different sizes. The element size is reduced as $l = l_0/N$, when N increases as a power of 2 ($N = 1, 2, 4, \ldots, 64$). The strain $\log(\epsilon_N/\epsilon_1)$ and effective stress $\log(\tau_N/\tau_1)$ are plotted in Fig. 5 as a function of $\log(N)$, where ϵ_N and τ_N are the stress and strain for resolution N, respectively, in the y-direction. Figure 5 shows that the stress and strain at the fracture tip follow the line $\frac{1}{2}\log(N)$, which can be used to scale the breaking threshold with respect to the element size.
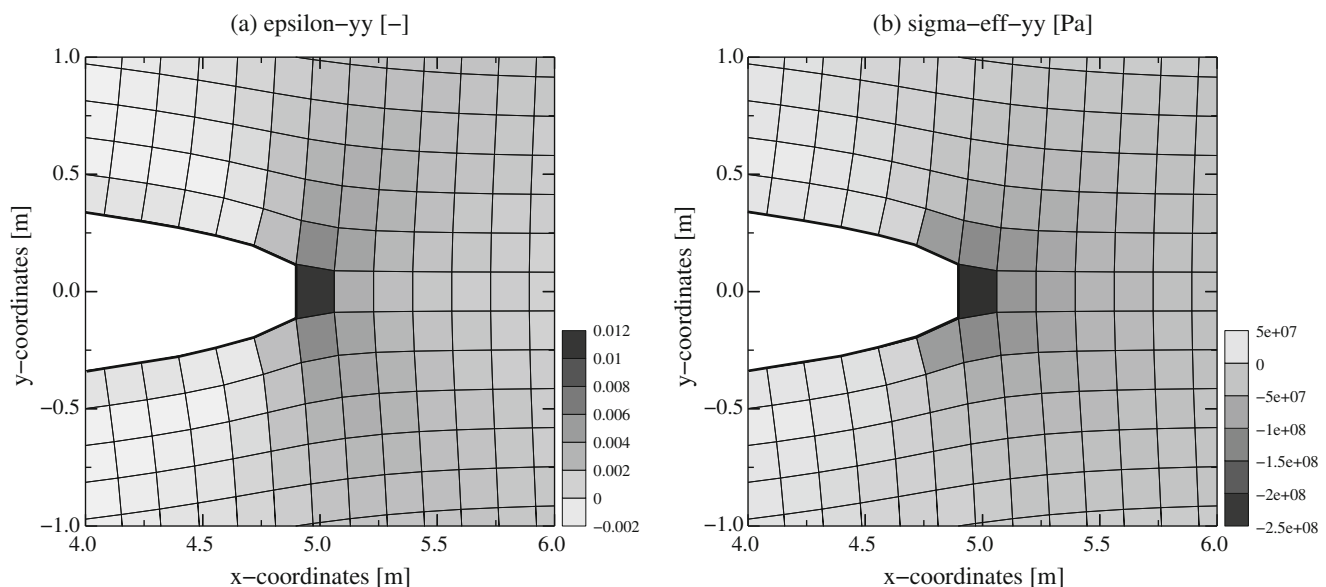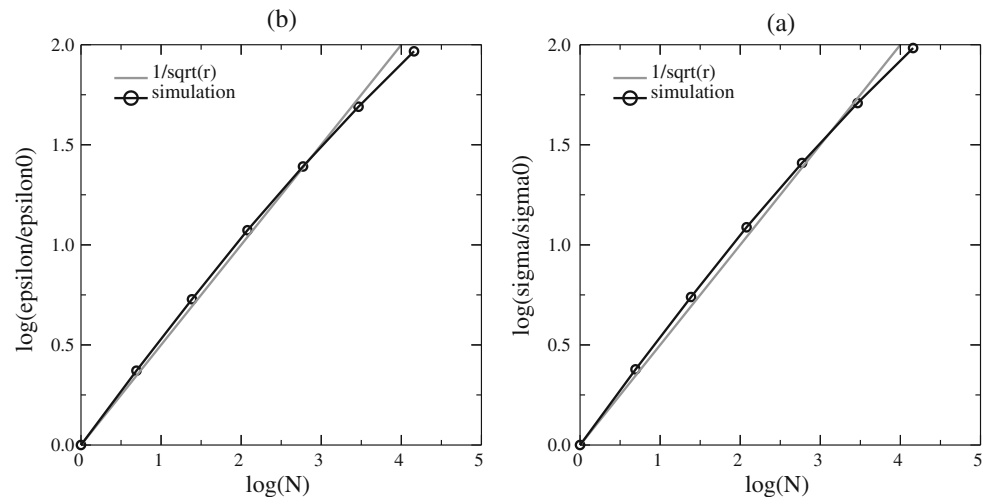

Fig. 4 Concentration of the stress in the element at the fracture tip. Only a part of the fracture is shown, and the displacement field is multiplied with a suitable factor to enlarge the deformations. The fracture center is at $x = 0$. **a** Strain ϵ_{yy}. **b** Stress σ_{yy}

Fig. 5 Stress enhancement at the fracture tip with increased grid resolution. **a** Strain $\log(\epsilon_{yy})$. **b** Stress $\log(\sigma_{yy})$

The scaling shown in Fig. 5 is consistent with the stress/strain singularity at the tip of a sharp fracture, where the stress is given as $\sigma_{yy} = K_{\mathrm{I}}/\sqrt{2\pi x}$, where K_{I} is the stress intensity factor, and x is a short distance from the fracture tip into the rock. Assuming that σ_N scales the same way, $\sigma_N \sim 1/\sqrt{l_0/N}$ gives that $\log(\sigma_N/\sigma_1) = \frac{1}{2}\log(N)$. The scaling of stress and strain shown in Fig. 5 for the element at the fracture tip is, therefore, the stress singularity of a sharp fracture in a linear elastic medium.

11 Homogeneous cases

The hydraulic fracture model is demonstrated in two cases: one is a homogeneous rock and the other is an inhomogeneous rock. The inhomogeneity is in terms of rock strength. The subsurface is represented by cube of size $2,075 \times 2,075 \times 2,075$ m³ where the injection point is at the center of the cube (at the depth $1,037.5$ m). The rock is gridded with two element sizes, where the volume $75 \times 75 \times 75$ m³ around the injection point is gridded with cells of size $5 \times 5 \times 5$ m³. The fracturing takes place in this inner cube. The grid surrounding the inner cube is represented with elements of the size $250 \times 250 \times 250$ m³. The larger elements serve to keep the boundaries away from the near-well area where fracturing takes place. Both cases have things in common on rock porosity $\phi = 0.2$, rock permeability $k = 1 \cdot 10^{-17}$ m², fluid viscosity $\mu = 1 \cdot 10^{-3}$ Pa s, fluid compressibility $c = 1 \cdot 10^{-8}$ Pa⁻¹, rock Young's modulus $E = 10$ GPa, fracture Young's modulus 0.5 Pa, Poisson ratio $\nu = 0.25$, and the injection rate $Q_{\mathrm{in}} = 100$ l min⁻¹. The injection starts at $t = 0$, and the rate is kept constant until the end of the experiments.

The homogeneous case has the same fracture criterion $\epsilon_{\mathrm{frac}} = 1/2 \cdot 10^{-4}$ for all cells of size 5 m. Figure 6

shows the fractures for the homogeneous case after 13 h of injection, where three orthogonal wings have propagated symmetrically away from the injection point. Figure 7a shows the well pressure (at the injection point) as a function of time. The number of broken elements in each event is plotted in Fig. 7b, and the elastic energy released during the events is shown in Fig. 7c. It should be noted that the elastic energy does not include the initial stress state—only the linear elastic stress. The number of broken elements becomes the new fracture surface area when it is multiplied with the area of an element side. Figure 7 shows that the fracture propagates in a few events, where a number of elements break in each event. The coloring of the fractured elements in Fig. 6 shows the time when the cells broke during propagation. The perimeter of the wings has acquired one new layer of cells during each fracture event. The distance away from the well, therefore, increases by one cell in the directions of the axes in each event. This is in agreement with the 2D model of Wangen [38] where
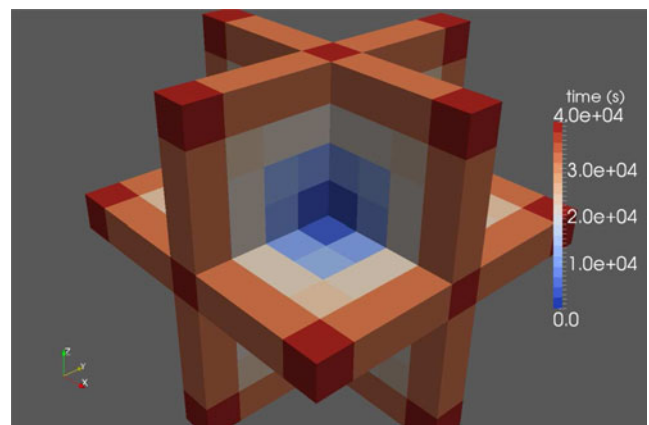

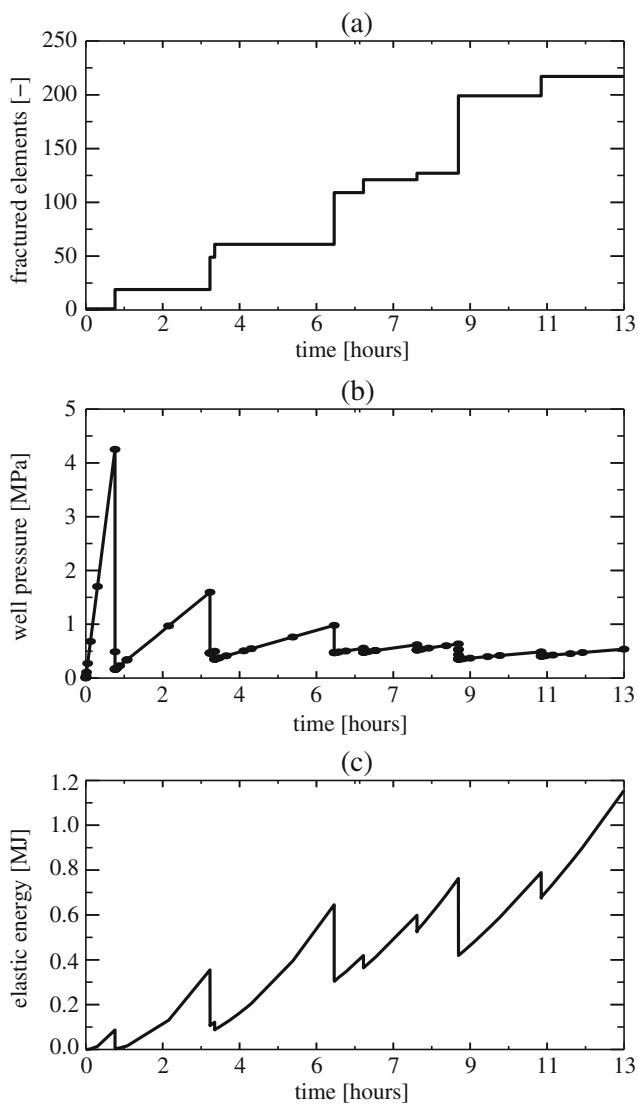**Fig. 6** The homogeneous case gives a symmetric fracture made by three orthogonal planes

Fig. 7 a Well pressure. **b** Number of broken elements. **c** Elastic energy stored in the grid

Figure 7a shows that the first fracture events require a pressure buildup followed by a substantial pressure drop. This is a grid-size effect. The injection point is a pre-fractured element, and a large pressure is needed to fracture the neighbors of this first element compared to the pressure needed to propagate a much larger fracture. The initial fracture becomes six times larger in size when the nearest neighbor elements break. This large expansion of the fracture creates the pressure drop. The pressure drops become smaller, and the well pressure becomes roughly flat with small oscillations after the initial pressure transients caused by the grid size effect. Figure 7 shows that the largest events have an energy release ~ 0.1 MJ, which corresponds to a moment magnitude a little less than ~ -2.5.

12 Inhomogeneous case

The second case is a demonstration of hydraulic fracturing in a heterogeneous rock, where the heterogeneity is made by assigning random strength to the elements. The strength is initialized at the beginning of the simulation, and it stays fixed (quenched disorder). The following distribution, taken from [33, 34], is used:

$$\epsilon_{\text{frac}} = \bar{\epsilon}_{\text{frac}} \frac{(r+2)}{(r+1)} \psi^{1/(r+1)} \qquad (24)$$

where ψ is a random variable uniformly distributed between 0 and 1, $\bar{\epsilon}_{\text{frac}} = 1/2 \cdot 10^{-4}$ is the average element strength, and the parameter r controls the width of the distribution. The distribution becomes narrow for large r, because $\epsilon_{\text{frac}} \to \bar{\epsilon}_{\text{frac}}$ when $r \to \infty$. A wide distribution is obtained with r close to -1, in which case some bonds get a strength in the neighborhood of $\bar{\epsilon}_{\text{frac}}$

the homogeneous case gave a linear fracture that grows symmetrically away from the well by the distance of a cell in each fracture event.

At this point, it should be mentioned that the time step is set to a minimum value when time stepping starts at $t = 0$ or restarts after a fracture event. The minimum time step is 1 s, and it is multiplied with the factor 2.5 after use. An increasing time step makes it possible to pick up pressure transients and at the same time do time stepping through long periods with no fracture events. The time steps used in the current case are marked by the bullets on the curve in Fig. 7a. Since the time steps are getting larger and larger until the fracture criterion is met, it implies that the time stepper goes beyond the exact time for the next event, which is when there is equality in the criterion (22).
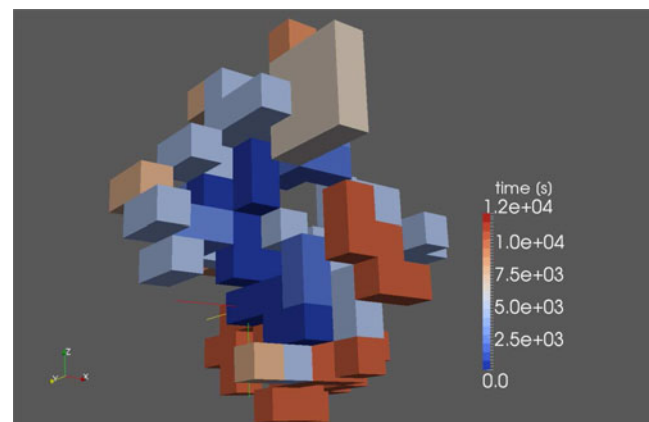

Fig. 8 The inhomogeneous case gives a branched fracture without any preferred fracture planes

and other bonds become very weak. The present case has $r = -0.5$ which gives strong heterogeneity.

Figure 8 shows the fracture pattern produced after 3 h of fluid injection. The strongly heterogeneous nature of the rock makes the fracture a disordered structure as it propagates away from the well. The fracture is not characterized by planar wings, but more by branched channels.

The well pressure, the number of broken elements in each event, and the corresponding energy released are plotted in Fig. 9. The inhomogeneous case shows the same initial pressure transients as the homogeneous case, which is a grid size effect. Then, a period follows with a slight increase in well pressure dominated by several fracture events, where each event breaks a small number of elements. The elastic energy released in the

heterogeneous case is smaller than in the homogeneous case.

The current two cases are end-members in terms of heterogeneity. Nevertheless, they have features in common, like an injection pressure that approaches a plateau, with pressure drops at the fracture events.

13 Conclusion

A 3D finite element formulation of hydraulic fracturing is suggested. The model partitions the stress into the initial stress and the additional stress caused by fluid injection. The latter (additional) rock stress is obtained as a solution of the Biot equations of coupled fluid flow and deformations.

It is shown how a uniform representation of the rock and the fracture are made for the pressure and the displacement equations. The elements of the fracture are different from the elements of the rock by means of porosity, permeability, source term, and Young's modulus. The fracture porosity is the volume fraction of fractures in an element, the fracture permeability accounts for the aperture, and the fracture elements have an almost zero Young's modulus. The aperture is obtained from the displacement field of the nodes at the fracture surface on the regular grid. The computed aperture is validated by a comparison with the exact ellipsoid solution for a linear elastic 3D medium.

The current formulation deals with tensile (mode I) fracture, and the initial stress state of the rock is, therefore, assumed isotropic. It should be straightforward to consider non-isotropic stress states and shear failure as well, although this is not yet tested. The maximum limit of the strain in each element is used as a fracture criterion. The strain maximum scales are shown numerically as one over the square root of the element size. When an element breaks, it changes status from rock to fracture.

A fracture event is followed by a pressure drop because the fluid pressure required to keep a large fracture open is less than for a small fracture when the volume of fluid in the fracture is constant. Fracturing is assumed to take place instantaneously, and the volume of fluid in the fracture is the same right after an event as it was right before.

The model is tested on two cases: a homogeneous rock and a heterogeneous rock. The homogeneous case gives a fracture front that propagates away from the injection point symmetrically along three orthogonal planes. All events in this case are at the front, and there are therefore no events in the interval between the front and the well. The rock strength can easily be
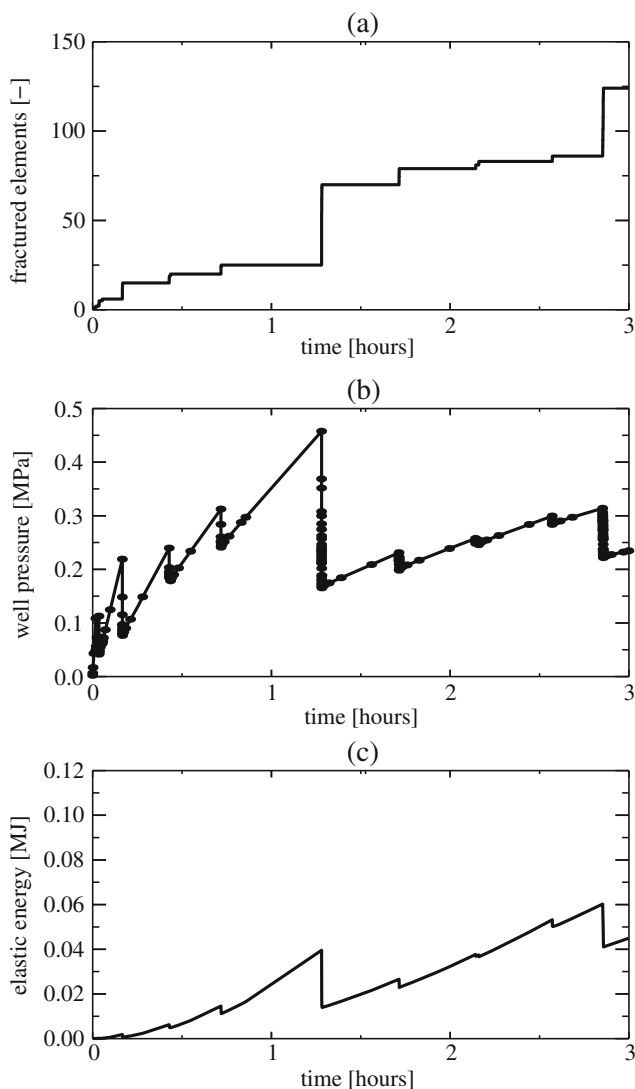

Fig. 9 **a** Well pressure. **b** Number of broken elements. **c** Elastic energy stored in the grid

made heterogeneous because there is a strength limit assigned to each element. The heterogeneous case gives a branched fracture, where there are events that fill the distance between the injection point and the farthest fracture tips. The well pressure, fracture surface, and the elastic energy released in each event are also computed. The well pressure has a gentle pressure increase with small pressure drops after a few initial pressure transients which related to the element size. The elastic energy released in the largest events is of the order 0.1 MJ when the well pressure is of the order 1 MPa. The homogeneous case gives fewer and larger events than the heterogeneous case.

Appendix: The finite element formulation

A multiplication of the force balance 1 with the basis function N_I associated with node I, and integration over the volume V gives

$$\int_V \frac{\partial \sigma_{ij}^{(1)}}{\partial x_j} N_I dV = \int_V \left(\frac{\partial \tau_{ij}^{(1)}}{\partial x_j} + \alpha \frac{\partial p^{(1)}}{\partial x_i} \right) N_I dV = 0 \quad (25)$$

in terms of effective stress $\tau_{ij}^{(1)}$. Upper case indices, like I and J, denote node numbers; and lower case indices i and j are spatial directions (Einstein summation convention is applied, which assumes summation over pairs of equal indices). The divergence theorem and partial integration of Eq. 25 give the Galerkin formulation

$$\int_V \tau_{ij}^{(1)} \frac{\partial N_I}{\partial x_j} dV - \int_{\partial V} \tau_{ij}^{(1)} n_j N_I dS = \int_V \alpha \frac{\partial p^{(1)}}{\partial x_i} N_I dV \quad (26)$$

The volume V has the surface ∂V with $\mathbf{n}$ as the outward pointing normal vector. The surface integral of $\tau_{ij}^{(1)}$ is zero because $\tau_{ij}^{(1)} = 0$ on the boundary. We impose zero displacement onto the equation system for the eight-corner nodes. The Galerkin formulation with the displacements as the unknowns becomes simplified by using the following standard notation [15, 23]. Stress and strain written as the vectors

$$\boldsymbol{\tau}^{(1)} = \left(\tau_{xx}^{(1)}, \ \tau_{yy}^{(1)}, \ \tau_{xy}^{(1)}, \ \tau_{xy}^{(1)}, \ \tau_{yz}^{(1)}, \ \tau_{xz}^{(1)} \right) \quad (27)$$

and

$$\boldsymbol{\epsilon} = \left(\epsilon_{xx}, \ \epsilon_{yy}, \ \epsilon_{zz}, \ 2\epsilon_{xy}, \ 2\epsilon_{yz}, \ 2\epsilon_{xz} \right) \quad (28)$$

allow for the compact notation

$$\begin{bmatrix} \tau_{1j} \dfrac{\partial N_I}{\partial x_j} \\[2mm] \tau_{2j} \dfrac{\partial N_I}{\partial x_j} \\[2mm] \tau_{3j} \dfrac{\partial N_I}{\partial x_j} \end{bmatrix} = \mathbf{B}_I^T \boldsymbol{\tau}^{(1)} \quad (29)$$

and

$$\boldsymbol{\epsilon} = \mathbf{B}_J \mathbf{u}_J \quad (30)$$

where derivatives of the basis function appear in the matrix.

$$\mathbf{B}_I^T = \begin{bmatrix} \dfrac{\partial N_I}{\partial x} & 0 & 0 & \dfrac{\partial N_I}{\partial y} & 0 & \dfrac{\partial N_I}{\partial z} \\[3mm] 0 & \dfrac{\partial N_I}{\partial y} & 0 & \dfrac{\partial N_I}{\partial x} & \dfrac{\partial N_I}{\partial z} & 0 \\[3mm] 0 & 0 & \dfrac{\partial N_I}{\partial z} & 0 & \dfrac{\partial N_I}{\partial y} & \dfrac{\partial N_I}{\partial x} \end{bmatrix} \quad (31)$$

The vector $\mathbf{u}_J = (u_{Jx}, u_{Jy}, u_{Jz})$ is the displacement in the x- and y-direction at node J. The Lamé Eq. 10 becomes $\boldsymbol{\tau}^{(1)} = \mathbf{D}\boldsymbol{\epsilon}$ when expressed with the stress and strain vectors, where $\mathbf{D}$ is the matrix.

$$\mathbf{D} = \begin{bmatrix} (2G+\lambda) & \lambda & \lambda & 0 & 0 & 0 \\ \lambda & (2G+\lambda) & \lambda & 0 & 0 & 0 \\ \lambda & \lambda & (2G+\lambda) & 0 & 0 & 0 \\ \hline 0 & 0 & 0 & G & 0 & 0 \\ 0 & 0 & 0 & 0 & G & 0 \\ 0 & 0 & 0 & 0 & 0 & G \end{bmatrix} \quad (32)$$

The Galerkin formulation (26) can now be re-expressed in terms of the displacements as

$$\int_V \mathbf{B}_I^T \mathbf{D} \, \mathbf{B}_J \mathbf{u}_J = \int_V \alpha \nabla p \, N_I dV \quad (33)$$

The pressure gradient on the right-hand side is the load that causes the displacements.

The pressure p_J^n is a solution of the following standard Galerkin formulation [15, 23]

$$\left(\int_V \phi c_f N_I N_J \, dV + \Delta t \int_V \frac{k}{\mu} \nabla N_I \nabla N_J \, dV \right) p_J^n \quad (34)$$

$$= \int_V C N_I N_J \, dV p_J^{n-1} + \Delta t \int_V Q \, N_I dV \quad (35)$$

which is obtained from the pressure Eq. 17 by multiplying by the basis function N_I and the use of Green's

theorem. The surface integral from Green's theorem drops out because of Dirichlet boundary conditions. Time discretization is backward Euler, where p^n and p^{n-1} are the pressures at the present and previous time step, respectively. The source term is

$$Q = \begin{cases} -\alpha\, \partial\epsilon/\partial t & \text{(rock elements)} \\ -\partial\phi_{\mathrm{F}}/\partial t & \text{(fracture element)} \end{cases} \qquad (36)$$

and the well element has, in addition, the injection rate $Q_{\mathrm{in}}/V_{\mathrm{E}}$. The equations for pressure and strain are solved, decoupled at each time step. The pressure equation is solved first. The pressure at the current time step is then used in the right-hand side of the equation for the displacements, which gives the displacements at the current time step. The possible instability caused by the source term (36), when the pressure and displacement equations are solved sequentially, is discussed in Section 6.

References

1. Al-Busaidi, A., Hazzard, J., Young, R.: Distinct element modeling of hydraulically fractured Lac du Bonnet granite. J. Geophys. Res. **110**(B06302), 1–14 (2005)
2. Alava, M., Nukala, P., Zapperi, S.: Statistical models of fracture. Adv. Phys. **55**, 349–476 (2006)
3. Bernabé, Y.: The transport properties of networks of crakcs and pores. J. Geophys. Res. **100**(B3), 4231–4241 (1995)
4. Biot, M.: General theory of three dimensional consolidation. J. Appl. Phys. **12**, 155–164 (1941)
5. Brown, S., Caprihan, A., Hardy, R.: Experimental observation of fluid flow in a single fracture. J. Geophys. Res. **103**(B3), 5125–5132 (1998)
6. Cheng, Y., Lee, W., McVay, D.: A new approach for reliable estimation of hydraulic fracture properties in tight gas wells. SPE Res. Eval. Eng. **12**(2): 254–262. SPE-105767-PA
7. Clifton, R.: Three-dimensional fracture-propagation models, chap. 5. In: Doherty, H.L. (ed.) Recent Advances in Hydraulic Fracturing. SPE Monograph Series, pp. 95–108. Memorial Fund of AIME, Society of Petroleum Engineers (1989)
8. Devloo, P., Fernandes, P., Gomes, S., Bravo, C., Damas, R.: A finite element model for three dimensional hydraulic fracturing. Math. Comput. Simul. **73**, 142–155 (2006)
9. Economides, M., Nolte, K.: Reservoir Stimulation, chap. 6, pp. 6.1–6.49. Wiley, New York (2000)
10. Evans, K., Moriya, H., Niitsuma, H., Jones, R., Phillips, W., Genter, A., Sausse, J., Jung, R., Baria, R.: Microseismicity and permeability enhancement of hydrogeologic structures during massive fluid injections into granite at 3 km depth at the Soultz HDR site. Geophys. J. Int. **160**(1), 388–412 (2005)
11. Flekkøy, E., Malthe-Sørenssen, A., Jamtveit, B.: Modeling hydrofracture. J. Geophys. Res. **107**(B8), ECV1-1–11 (2002)
12. Geertsma, J.: Two-dimensional fracture propagation models, chap. 4. In: Doherty, H.L. (ed.) Recent Advances in Hydraulic Fracturing, SPE Monograph Series, pp. 81–94. Memorial Fund of AIME, Society of Petroleum Engineers (1989)
13. Gidley, J.: Recent advances in hydraulic fracturing, SPE monograph series. In: Doherty, H.L. (ed.) Memorial Fund of AIME. Society of Petroleum Engineers (1989). http://books.google.no/books?id=sT5jQgAACAAJ
14. Herrmann, J., Roux, S.: Statistical models for the fracture of disordered media. North-Holland, Amsterdam (1990)
15. Huyakorn, P., Pinder, G.: Computational Methods in Subsurface Flow. Academic, New York (1983)
16. Jackson, M., Cheadle, M., Atherton, M.: Quantitative modeling of granitic melt generation and segregation in the continental crust. J. Geophys. Res. **108**(B7), 1–21 (2003)
17. Jaeger, J., Cook, N., Zimmerman, R.: Fundamentals of Rock Mechanics, 4th edn. Blackwell Scientific Publications, London (2007)
18. Judd, A., Hovland, M.: Seabed fluid flow. Impact on Geology, Biology and the Marine Environment. Cambridge University Press, Cambridge (2007)
19. Kim, J., Tchelepi, H., Juanes, R.: Stability, accuracy and efficiency of sequential methods for coupled flow and geomechanics. SPE J. **119084**, 249–262
20. Kramer, D.: Shale-gas extraction faces growing public and regulatory challenges. Phys. Today **64**(7), 23–25 (2011)
21. Kvamme, B., Liu, S.: Reactive transport of CO2 in saline aquifers with implicit geomechanical analysis. Energy Procedia **1**, 3267–3274 (2009)
22. Lam, K., Cleary, M.: Three-dimensional analysis of hydraulic fracturing. Comput. Geotech. **3**, 213–228 (1987)
23. Langtangen, H.: Computational partial differential equations: numerical methods and diffpack programming. Springer, Berlin (1999)
24. Rector, J., Qicheng, D., Patzek, T.: Passive characterization of hydrofracture properties using signals from hydraulic pumps. J. Pet. Sci. Eng. **27**, 49–58 (2000)
25. Rozhko, A.: Role of seepage forces on seismicity triggering. J. Geophys. Res. **115**(B11314), 1–12 (2010)
26. Rutqvist, J., Tsang, C.-F.: A study of caprock hydromechanical changes associated with CO2-injection into a brine formation. Environ. Geol. **42**, 296–305 (2002)
27. Sanjuan, B., Pinault, J.-L., Rose, P., Gérard, A., Brach, M., Braibant, G., Crouzet, C., Foucher, J.-C., Gautier, A., Touzelet, S.: Tracer testing of the geothermal heat exchanger at Soultz-sous-Forêts (France) between 2000 and 2005. Geothermics **35**, 622–653 (2006)
28. Sasaki, S.: Characteristics of microseismic events induced during hydraulic fracturing experiments at the Hijiori hot dry rock geothermal energy site, Yamagata, Japan. Tectonophysics **289**, 171–188 (1998)
29. Shapiro, S.A., Dinske, D.: Scaling of seismicity induced by nonlinear fluid-rock interaction. J. Geophys. Res. **114**(B09307), 1–14 (2009)
30. Shapiro, S.A., Dinske, D., Rothert, E.: Hydraulic-fracturing controlled dynamics of microseismic clouds. Geophys. Res. Lett. **33**(L14312), 1–5 (2006)
31. Sibson, R.: Implications for fault-valve behaviour for rupture nucleation and recurrence. Tectonophysics **211**, 283–293 (1992)
32. Turcotte, D., Morgan, J.: The physics of magma migration and mantle flow beneath a mid-ocean ridge, Geophysical Monograph. AGU **71**, 151–182 (1992)
33. Tzschichholz, F., Herrmann, H.: Simulations of pressure fluctuations and acoustic emission in hydraulic fracturing. Phys. Rev. **E51**, 1961–1970 (1995)
34. Tzschichholz, F., Herrmann, H., Roman, H.P.M.: Beam model for hydraulic fracturing. Phys. Rev. **B49**, 7056–7059 (1994)

35. Tzschichholz, F., Wangen, M.: Modelling of hydraulic fracturing of porous materials, pp. 227–260. WIT, Southhampton (1998)

36. Wang, H.: Theory of linear poroelasticity. Princeton University Press, Princeton (2000)

37. Wangen, M.: A quantitative comparison of some mechanisms generating overpressure in sedimentary basins. Tectonophysics **334**, 211–234 (2001)

38. Wangen, M.: Finite element modelling of hydraulic fracturing on a reservoir scale in 2D. J. Pet. Sci. Eng. **77**, 274–285 (2011)

39. Weng, X., Settari, A., Keck, R.: A field demonstration of hydraulic fracturing for solid waste diposal—injection pressure analysis. Int. J. Rock Mech. Min. Sci. **34**(3–4), 331.e1–331.e17 (1997). doi:10.1016/S1365-1609(97)00212-8